

Mixed Chalcogenide-Halides for Stable, Lead-Free and Defect-Tolerant Photovoltaics: Computational Screening and Experimental Validation of CuBiSCl_2 with Ideal Band Gap

Chen Ming, Zhizhong Chen, Fan Zhang, Shuiping Gong, Xiaowei Wu, Jie Jiang, Tang Ye, Qing Xu, Ke Yang, Liang Wang, Xun Cao, Songwang Yang,* Shengbai Zhang, Yong Zhang,* Jian Shi,* and Yi-Yang Sun*

Lead halide perovskites have emerged as promising photovoltaic (PV) materials owing to their superior optoelectronic properties. However, they suffer from poor stability and potential toxicity. Here, computational screening with experimental synthesis is combined to explore stable, lead-free, and defect-tolerant PV materials. Heavy cations with lone-pair electrons and mixed anions of chalcogens and halogens as a descriptor for simultaneous realization of defect tolerance and high stability are adopted. Together with the criteria of possessing direct band gap and optimal gap value, the inorganic material database is screened and CuBiSCl_2 in the post-perovskite structure is identified with an ideal band gap of 1.37 eV. The electronic structure and defect calculations suggest its defect-tolerant characteristics. By optical absorption measurement, its band gap is confirmed to be ≈ 1.44 eV, with strong absorption near the band edge. The material is stable against thermal decomposition up to 300 °C and can survive from 25 days of storage at ambient conditions with 60% relative humidity. Prototype solar cells are fabricated and demonstrate an open circuit voltage of 1.09 V and a power conversion efficiency of 1.00%. With the excellent properties above, CuBiSCl_2 is proposed to be a promising candidate for PV application.

1. Introduction

In the past decade, the photovoltaic (PV) community has witnessed a rapid development of lead halide perovskite (LHP) materials.^[1] Since 2009, the power conversion efficiency (PCE) of LHPs has been dramatically improved from the initial 3.8% to the recently certified value of 25.5%,^[2,3] which is unprecedented in the history of this field. The low fabrication cost is another main attraction of LHPs, as simple solution synthesis methods can be used to prepare the LHP layers in the solar cells without sacrificing the high efficiency.^[4,5] Other than PV, LHPs have also been successfully applied to light-emitting^[6,7] and photodetection devices.^[8,9] Despite the great potential, industrial adoption of LHPs still faces two critical challenges, i.e., the poor long-term stability and potential toxicity from the element lead (Pb). Stable and lead-free perovskites are thus highly desired for PV.^[10–13]

C. Ming, X. Wu, Q. Xu, L. Wang, X. Cao, Y.-Y. Sun
State Key Laboratory of High-Performance Ceramics
and Superfine Microstructure
Shanghai Institute of Ceramics
Chinese Academy of Sciences
Shanghai 201899, China
E-mail: yysun@mail.sic.ac.cn

Z. Chen, J. Jiang, J. Shi
Department of Materials Science and Engineering
Rensselaer Polytechnic Institute
Troy, NY 12180, USA
E-mail: shij4@rpi.edu

F. Zhang, T. Ye, Y. Zhang
Department of Electrical and Computer Engineering
University of North Carolina at Charlotte
Charlotte, NC 28223, USA
E-mail: yong.zhang@uncc.edu

F. Zhang
Songshan Lake Materials Laboratory
Dongguan, Guangdong 523808, China

S. Gong, S. Yang
CAS Key Laboratory of Materials for Energy Conversion
Shanghai Institute of Ceramics
Chinese Academy of Sciences
Shanghai 201899, China
E-mail: swyang@mail.sic.ac.cn

K. Yang, S. Zhang
Department of Physics
Applied Physics and Astronomy
Rensselaer Polytechnic Institute
Troy, NY 12180, USA

 The ORCID identification number(s) for the author(s) of this article can be found under <https://doi.org/10.1002/adfm.202112682>.

DOI: 10.1002/adfm.202112682

The replacement of Pb by its neighboring elements in the periodic table, such as Sn, Bi and Sb, is among the most extensively studied approaches. Sn and Pb belong to the same group and exhibit similar chemical properties. Replacing Pb by Sn can preserve the perovskite structure and the optoelectronic properties to some extent.^[14] However, the stability of Sn-based perovskites is usually even worse than the Pb-based ones due to the intrinsic instability of Sn²⁺. Replacing Pb by heterovalent elements Bi and Sb needs to balance the charge, e.g., in double perovskites. Possible combinations of cations in double perovskites have been screened by computations^[15,16] and some stable candidates such as Cs₂AgBiX₆ (X = Cl or Br) have been synthesized.^[17] However, these materials usually exhibit indirect and large band gaps,^[18] resulting in low PCE. Dimension reduction has also been proposed as a strategy to replace Pb. By using the low-dimensional perovskite structures, such as Ruddlesden-Popper compounds A₂Sn(Ge)X₄^[19,20] or layered compounds A₃Bi(Sb)₂X₉ (X = Cl or Br),^[21,22] significantly enhanced stability has been realized. But the low dimensionality breaks the connectivity of octahedra and leads to the large band gap and large exciton binding energy, limiting the performance (PCE <10%).^[10] Inspired by LHPs, chalcogenide perovskites have been explored as lead-free PV and optoelectronic materials.^[23–30] Based on computational screening, promising compounds such as BaZrS₃ have been predicted.^[23] They have also been confirmed experimentally to be direct band gap materials with strong absorption at the band edge and have high stability, but no PV devices have been demonstrated yet.^[24,27] Despite these efforts, the reported lead-free perovskite materials are still not on par with the LHPs so far in terms of PCE.

Though the current explorations primarily focus on the perovskite structure, the scope can be expanded to perovskite-derived structures or non-perovskite structures inspired by the physical insights behind the excellent performance of LHPs. Two of the most attractive features of LHPs are the high optical absorption and defect tolerance. Defect tolerance plays a central role in the observed ultralong lifetime of the photo-excited carriers even under the existence of possible defects due to the solution processing.^[31] The defect tolerance in LHPs is believed to originate mainly from their unique band structures and good dielectric properties. The valence band maximum (VBM) of the LHP exhibits an antibonding feature from interaction of the lone-pair Pb-s state and the halogen p states. This is different from common semiconductors, where the VBM shows a bonding feature. The conduction band minimum (CBM) is mainly composed of the unoccupied Pb-p states.^[32,33] Due to the strong spin-orbit coupling (SOC) effect in Pb, the degenerate CBM in LHPs is split and the band edge is downshifted substantially.^[34,35] These unique features of the band structure give rise to shallow defect levels for most intrinsic defects in LHPs, which are responsible for defect tolerance.^[31,33,36–40]

LHPs also feature strongly polarized bonds, which give rise to the large dielectric constants.^[41,42] The large dielectric constant screens the attraction between the photo-excited electrons and holes and contributes to the long carrier lifetime.^[43] The strongly polarized bonds are related to weakness of the bonding in LHPs and the softness of the materials, which necessarily leads to low structure stability, particularly under moist environment.

To enhance stability, mixing chalcogen into halides might be a useful strategy. As the chalcogen anions have higher valence, the bonding is expected to be stronger than that in pure halides giving rise to enhanced stability, which has been demonstrated by good stability of the chalcogenide perovskites.^[44–46]

Inspired by the analysis above, we propose several design criteria for PV materials: (1) utilization of cations with large atomic numbers and lone pairs as cations, (2) mixed chalcogen and halogen as anions, (3) optimal direct band gaps. There have been several reports on related materials for PV applications. Using first-principles calculations, mixed chalcogenide-halide perovskites (e.g., CH₃NH₃BiSeI₃),^[47] and mixed-anion non-perovskite compounds SbS(Se)I₃^[48] have been proposed to be promising PV materials. Experimentally, it has been claimed that mixed chalcogenide-halide compounds MASbSI₂ can achieve PCE exceeding 4%,^[49] even though later it was argued that the material synthesized may contain binary or ternary compounds.^[50] PCEs of ≈4% have also been obtained based on the sulfoiodides Sb(Bi)SI.^[51,52] A recent review has also pointed out potential applications of mixed-anion compounds.^[53] These previous studies suggest that a systematic search is required to further explore the mixed chalcogenide-halides for photovoltaics.

In this work, we combined the computational screening and experimental synthesis to explore the stable and lead-free PV materials with defect tolerance based on the mixed chalcogenide-halide compounds. Using the criteria above and accurate band gap calculation at HSE+SOC level, we screened all the possible compounds in the Materials Project (MP) database^[54] and identify CuBiSCL₂ as the most promising one with an ideal band gap of 1.37 eV. Focusing on this material, we then performed detailed electronic structure and defect calculations and verified its defect tolerance. We further synthesized CuBiSCL₂ and observed strong optical absorption of above 10⁴ cm⁻¹ near the band edge with the measured band gap in good agreement with the calculations. It is stable up to 300 °C against thermal decomposition and can survive for 25 days stored at room temperature in air with 60% relative humidity. We also fabricated solar cells using CuBiSCL₂ as the light absorber. As a demonstration, without optimizing the device parameters, we have found that the device can have a PCE of 1.00% and an open circuit voltage of 1.09 V. Our results suggest CuBiSCL₂ to be a promising stable and lead-free material for PV applications. Moreover, our results indicate that the mixed anion perovskites could be a direction worthy of exploration for lead-free PV materials.

2. Results and Discussion

Figure 1a shows the schematic of the screening process. The targeted materials should contain cations with large atomic numbers and lone pairs (In, Sn, Sb, Bi), and anions with both chalcogen (S, Se, Te) and halogen (Cl, Br, I). With these criteria, 193 compounds were found in the MP database. Eliminating the compounds with toxic elements, such as Pb, Tl and Hg and magnetic elements, such as Mn and Ni, 176 compounds were left. It should be noted that we did not limit the screening to perovskite structures.

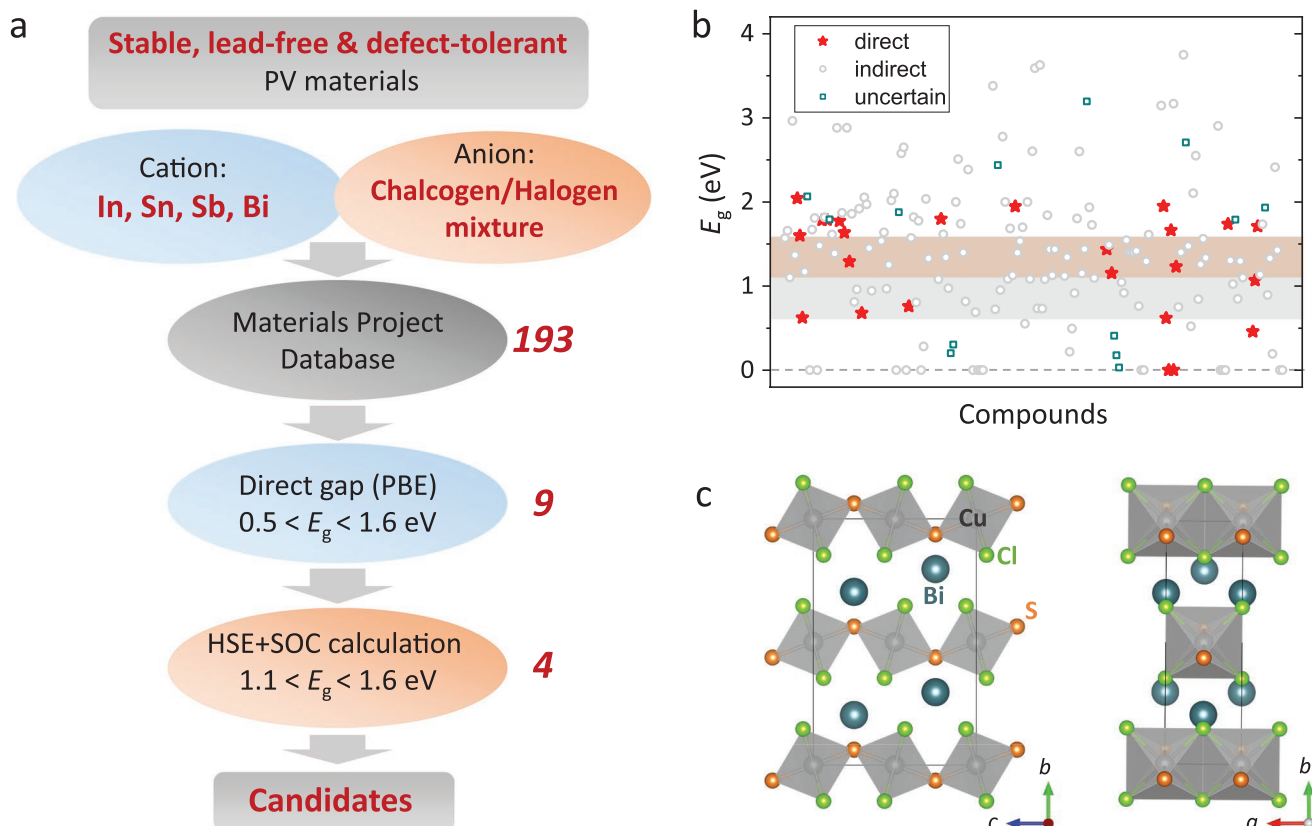


Figure 1. a) Schematic of the screening process. b) Calculated band gaps of 176 compounds based on the PBE functional. The stars and circles denote the compounds with direct and indirect band gaps, respectively. The squares denote the compounds with unknown types of band gap, whose gap values are out of the optimal region. c) Atomic structure of $\text{CuBiS}_2\text{Cl}_2$.

With these compounds, we performed further screening based on the criterion of being direct band gap with optimal gap values. The accurate prediction of band gap is essential to the screening of PV materials. As we mainly focused on the compounds with heavy anions where the SOC effect is strong, hybrid functional with the inclusion of SOC is required to accurately describe the electronic structures as previously shown in LHPs.^[31,33] To reduce the computation cost, we used a hierarchical strategy, i.e., using the PBE functional to coarsely screen the compounds with the direct gaps and optimal gap values, then HSE+SOC is used to obtain a more accurate band gap. For those compounds, whose full band structures are unavailable in the MP database, we performed PBE calculations to judge if the gap is direct and if it is inside the optimal region. According to the Shockley-Queisser theory,^[55] the optimal region of gaps was selected to be ≈ 1.1 – 1.6 eV for the HSE+SOC calculation. As the PBE functional is known to underestimate the band gap, the region for the coarse screening was broadened to ≈ 0.5 – 1.6 eV.

Figure 1b shows the calculated gap values of 176 compounds by PBE. It can be seen that most compounds show an indirect gap. There are 81 compounds with band gap within ≈ 0.5 – 1.6 eV, but only 9 compounds exhibit direct gap, which were listed in **Table 1**. Further HSE+SOC screening yielded four final compounds, which are $\text{CuBiS}_2\text{Cl}_2$, $\text{In}_2\text{Bi}_3\text{Se}_7\text{I}$, $\text{In}_2\text{CuTe}_3\text{Cl}$ and $\text{In}_2\text{CuTe}_3\text{I}$ with band gaps of 1.37, 1.41, 1.26 and 1.21 eV, respectively. The atomic and band structures of the selected

compounds were shown in Figures S1 and S2 (Supporting Information). Among the selected compounds, $\text{CuBiS}_2\text{Cl}_2$ exhibits the ideal band gap. Its constituent elements are all earth-abundant, which may ensure low cost for fabrication. We, therefore, focused on $\text{CuBiS}_2\text{Cl}_2$ in the rest of this work.

The structure of $\text{CuBiS}_2\text{Cl}_2$ with space group $Cmcm$ is shown in Figure 1c. Cu cations sit at the centers of the dual-anion octahedra, which form layers separated by the Bi cations. If the anions are all the same, the structure is referred to as a “post-perovskite” structure, as it was discovered that under high

Table 1. The obtained compounds by screening and their calculated band gaps (in eV) by the PBE and HSE+SOC calculations.

Formula	E_g^{PBE}	$E_g^{\text{HSE+SOC}}$
$\text{CuBiS}_2\text{Cl}_2$	0.67	1.37
$\text{AgBiS}_2\text{Cl}_2$	1.10	1.67
$\text{Sn}_5(\text{S}_2\text{Cl})_2$	0.59	0.52
InSeI	1.42	2.13
$\text{In}_2\text{Bi}_3\text{Se}_7\text{I}$	1.14	1.41
$\text{Bi}_3(\text{TeCl}_5)$	1.18	1.72
$\text{Ga}_2\text{SbTe}_4\text{Cl}_7$	1.22	1.70
$\text{In}_2\text{CuTe}_3\text{Cl}$	0.61	1.26
$\text{In}_2\text{CuTe}_3\text{I}$	0.63	1.21

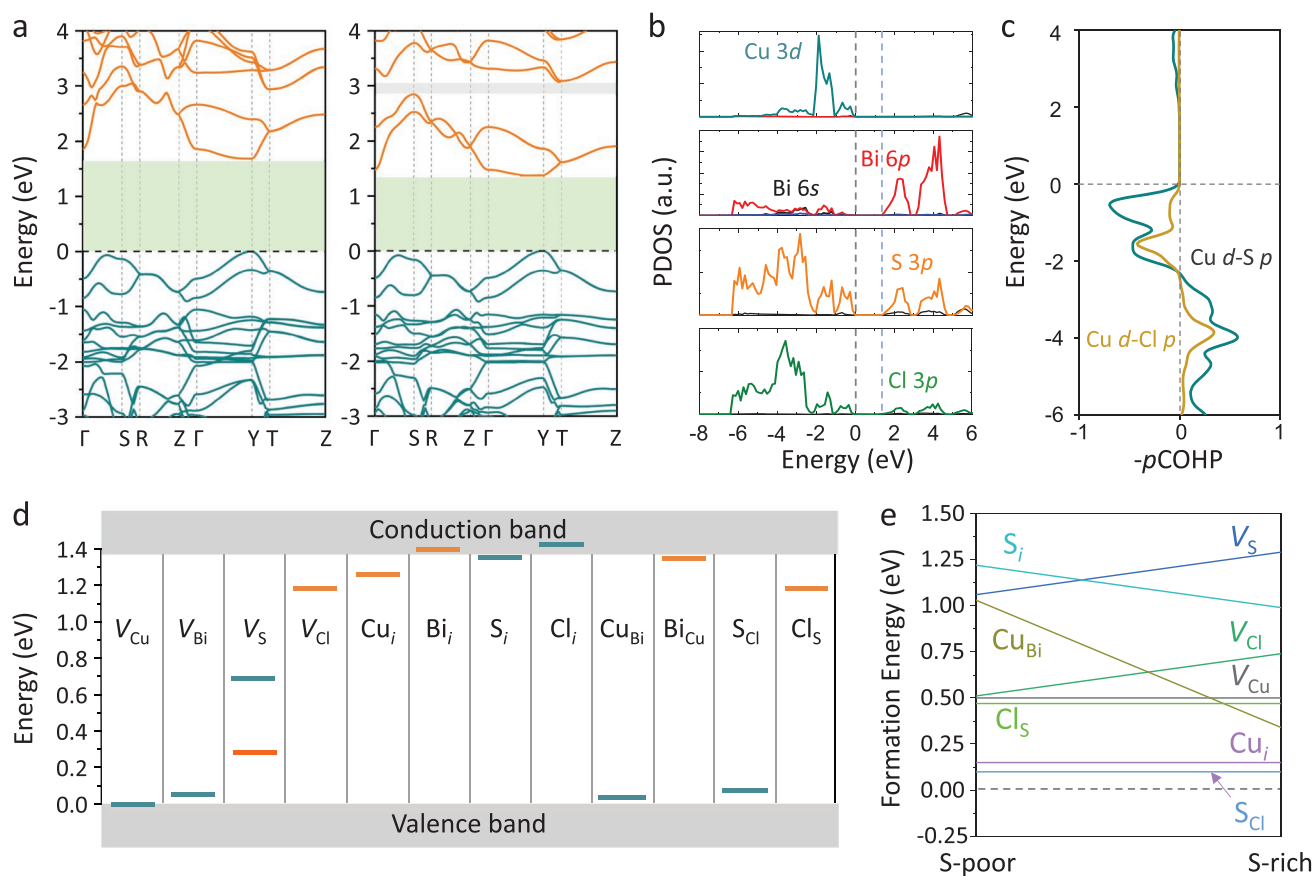


Figure 2. a) Band structures of $\text{CuBiS}_2\text{Cl}_2$ calculated by HSE (left) and HSE+SOC (right). b) Projected density of states of $\text{CuBiS}_2\text{Cl}_2$ calculated by HSE+SOC. c) Projected crystal orbital Hamilton populations of the band edge on the Cu–S and Cu–Cl interactions. d) Transition levels and e) formation energies of intrinsic defects in $\text{CuBiS}_2\text{Cl}_2$. The orange and cyan bars in (d) denote the $\epsilon(+/0)$ and $\epsilon(0/-)$ levels, respectively. The defects with the formation energy below 1.5 eV were shown in (e).

pressure the perovskite material MgSiO_3 undergoes a phase change to this $Cmcm$ structure.^[56,57] In $\text{CuBiS}_2\text{Cl}_2$, however, the anion sites (i.e., the corners of the octahedra) are shared by S and Cl, representing a mixed anion (or split anion) compound.^[47,53] Note that the crystal structure of $\text{CuBiS}_2\text{Cl}_2$ has been reported in the literature,^[58] but its optical properties have not been studied yet.

Figure 2a compares the band structures of $\text{CuBiS}_2\text{Cl}_2$ obtained without and with the SOC effect based on HSE calculations. Without SOC, it yields a direct gap of 1.68 eV with both the CBM and VBM located at the Y point. Strong SOC can be clearly seen from the comparison as the conduction band is split into a lower and an upper band, which are separated by a gap of ≈ 0.2 eV as marked by a gray ribbon. The splitting pushes down the CBM by 0.31 eV and the band gap is reduced to 1.37 eV. Switching on SOC shifts the CBM from Y toward the Γ point, but the energy difference between the CBM and the state at Y point is small (10 meV). This quasi-direct band gap is expected to exhibit strong absorption with an ideal gap for PV applications. The effective mass of $\text{CuBiS}_2\text{Cl}_2$ exhibits an anisotropic feature as shown in **Table 2**. Along the c -axis as labeled in **Figure 1c**, both of the effective masses of electron ($0.41 m_0$) and hole ($1.07 m_0$) are moderate indicating that the transport should be optimal in this direction.

As seen from **Figure 2b**, the CBM is mainly composed of Bi- p states (see also from the charge density in **Figure S3**, Supporting Information). This explains the strong splitting of the conduction band, as the SOC effect is strong for the $6p$ orbital of Bi. The VBM is a hybrid state between Cu- $3d$, S- $3p$, and Cl- $4p$ states, while the lone-pair Bi- s state was buried in the valence band (**Figure 2b**). This should be the result of the p - d repulsion between the orbitals of Cu and S/Cl atoms, which pushes the antibonding states up substantially. Using the crystal orbital Hamilton populations (COHP) analysis,^[59] we verified this p - d repulsion picture and confirmed the anti-bonding feature of the VBM (see **Figure 2c**). Thus, $\text{CuBiS}_2\text{Cl}_2$ indeed exhibits the required band features as targeted by the screening, which could lead to shallow defect transition levels. In addition, the static dielectric permittivity ϵ_0 of $\text{CuBiS}_2\text{Cl}_2$ is calculated to be

Table 2. Effective masses of $\text{CuBiS}_2\text{Cl}_2$ along different directions. The unit of effective mass is m_0 .

	e	h
m_x	0.23	3.76
m_y	6.04	0.5
m_z	0.41	1.07

33.3, which is mainly contributed by the ionic part as high-frequency dielectric permittivity ϵ_∞ is only 8.7. Even though this value is smaller than that of LHPs (≈ 70), it is three times that of Si (11.7) and $\text{Cu}_2\text{ZnSnS}_4$ (≈ 10).^[60] The combination of the unique band features together with the large dielectric constants of CuBiSCl_2 is expected to give rise to high defect tolerance similar to that of LHPs.

To further verify the defect tolerance of CuBiSCl_2 , we studied the properties of the intrinsic defects. Figure 2d shows the calculated defect transition levels $\epsilon(0/-)$ and $\epsilon(+/0)$ by $\epsilon(0/-) = E_D^- - E_D^0 - E_{VBM}$ and $\epsilon(+/0) = E_D^0 - E_D^+ - E_{VBM}$ at the HSE+SOC level (see Experimental Section), where E_D^q is the total energy of the supercell containing a defect in the charge q state and E_{VBM} is the energy of the VBM. We considered the neutral or singly charged defects, because in these charge states the defects could easily serve as recombination centers.^[37,61] As shown in Figure 2d, the defect transition levels are indeed mostly shallow, except for the S vacancy (V_S), which has the $\epsilon(+/0)$ level located in the middle of the gap indicating that V_S could be a potential recombination center in this material. To evaluate the concentration of V_S , we calculated the defect formation energy at different synthesis conditions (see Experimental Section and Figure S4, Supporting Information for details). As

shown in Figure 2e, V_S has a formation energy varying from 1.06 eV under S-poor condition to 1.29 eV under S-rich condition. This value is much larger than that of the iodine interstitial in MAPbI_3 (≈ 0.3 eV),^[31] which is considered to be the major recombination center therein. From Figure 2e, S-on-Cl anti-site (S_{Cl}) and Cu interstitial (Cu_i) have formation energy as low as 0.1 eV, indicating that these defects are easily formed in this material. As shown in Figure 2d, these two defects have shallow transition levels and do not serve as efficient recombination centers.

We synthesized CuBiSCl_2 by solid-state reactions, as detailed in the Experimental Section. Figure 3a shows a chunk of the crystal. The material appears in black indicating good absorption of visible light. Figure 3b shows the X-ray diffraction (XRD) pattern, which is compared with the simulated pattern using the computationally optimized structure. The compared structural parameters were given in Tables S1 and S2 (Supporting Information). The excellent agreement between the two patterns confirms the synthesis of CuBiSCl_2 in the post-perovskite structure. Figure 3c shows the scanning electron microscope (SEM) image of a piece of CuBiSCl_2 sample, which consists of slab-shaped grains with a typical thickness of several tens of μm and typical width over 100 μm (see also in Figure S6,

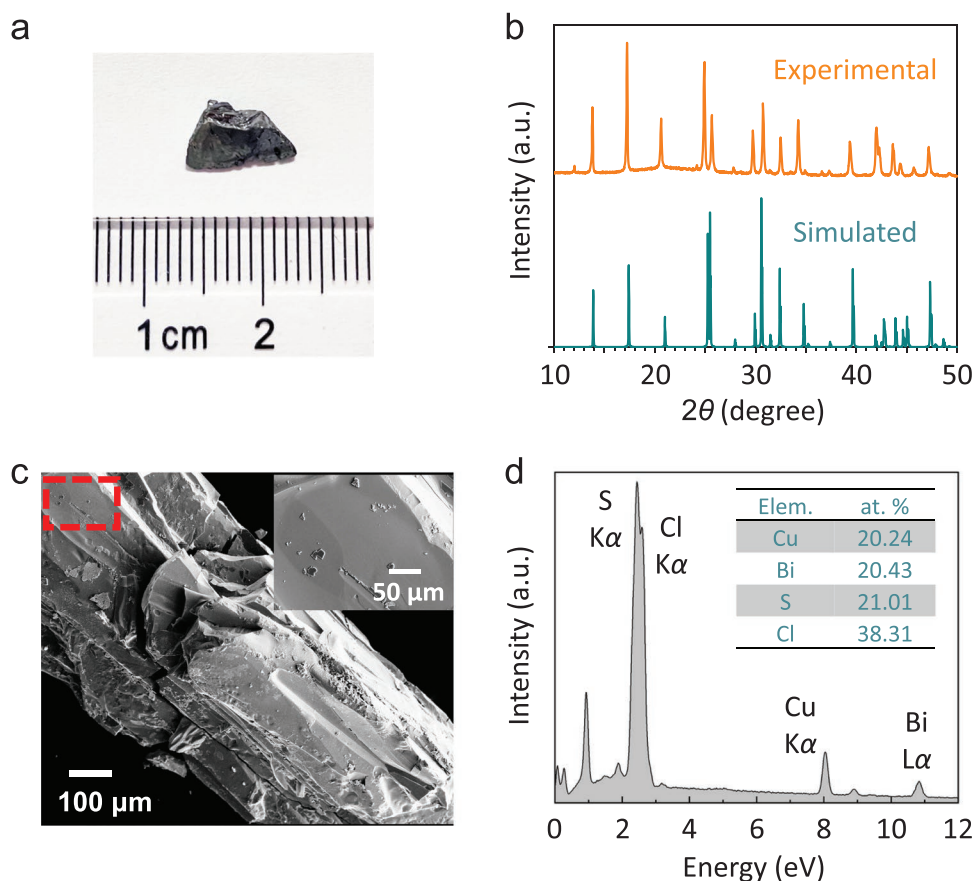


Figure 3. a) Photograph of as-grown sample of CuBiSCl_2 . b) XRD pattern of CuBiSCl_2 , compared with the simulated pattern using the computationally optimized structure. c) SEM image on a piece of CuBiSCl_2 sample. The inset shows the red-color framed area with higher magnification. d) EDX spectrum obtained from the framed area in (c). The inset shows the determined elemental ratio.

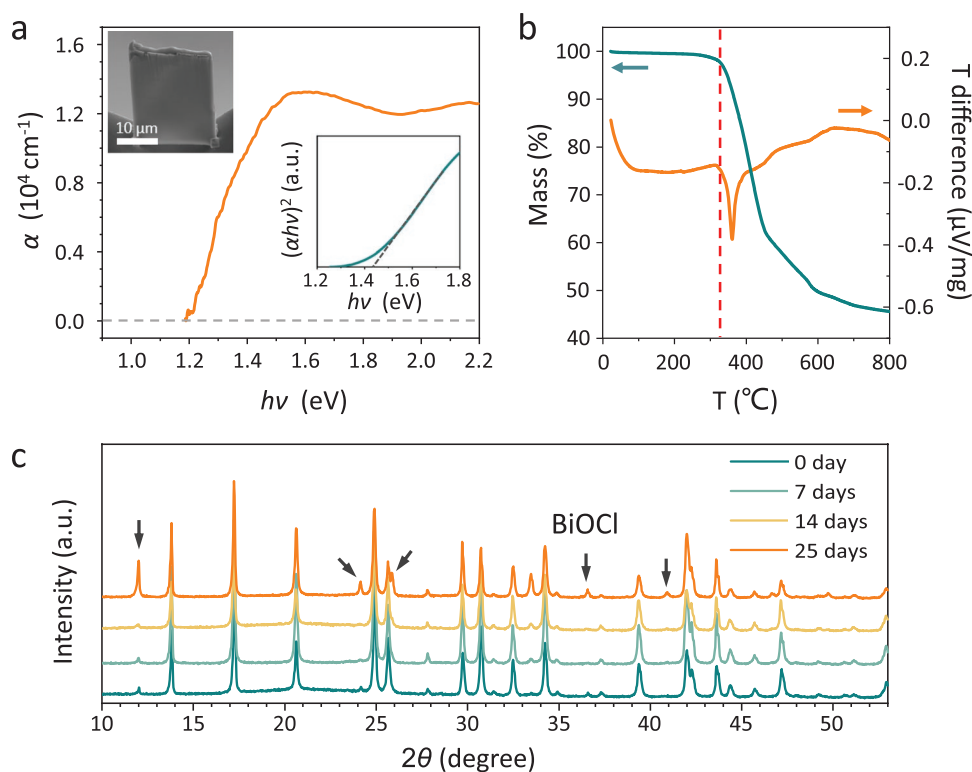


Figure 4. a) Measured optical absorption spectrum of $\text{CuBiS}_2\text{Cl}_2$. The top-left inset shows the thin film used for the measurement with a size of $20 \times 20 \times 3 \mu\text{m}$, which is cut from a large chunk sample by focused ion beam. The bottom-right inset shows the Tauc plot for determining the band gap. b) TGA/DTA measurements on the thermal stability of $\text{CuBiS}_2\text{Cl}_2$. The powder sample was heated from 20 to 800°C with a heating rate of $10.0^\circ\text{C min}^{-1}$ in nitrogen atmosphere and a flow rate of 20 ml min^{-1} . c) Evolution of XRD patterns for the $\text{CuBiS}_2\text{Cl}_2$ samples stored at room temperature in air with 60% relative humidity. The black arrows mark the peaks attributed to the compound BiOCl .

Supporting Information). The inset of Figure 3c shows a flat surface, on which energy dispersive X-ray (EDX) analysis was carried out. As shown in Figure 3d, the elemental ratio is close to stoichiometry.

To evaluate the optical absorption properties, we used a focused ion beam (FIB) to cut a $3 \mu\text{m}$ thick $\text{CuBiS}_2\text{Cl}_2$ film with lateral dimension of $\approx 20 \times 20 \mu\text{m}$ as shown in the inset of Figure 4a. The optical absorption was then measured on the film by a transmission setup (see Experimental Section). As seen in Figure 4a, the measured absorption spectrum shows that from ≈ 1.4 to 2.2 eV , the optical absorption coefficient varies between 1.0×10^4 to $1.3 \times 10^4 \text{ cm}^{-1}$. The optical bandgap is estimated to be 1.44 eV from the Tauc plot, as shown in the inset of Figure 4a, which is in good agreement with the HSE+SOC calculation. We also measured the optical absorption directly from the as-grown material by selecting the edge region of a thin sample. The obtained optical band gaps are close to that of the FIB-cut sample (see Figure S7, Supporting Information).

Stability with respect to temperature and moisture is a critical concern for PV applications. In order to address the stability issue of LHPs, we proposed to use anions with mixed chalcogen and halogen in this work. It is expected that $\text{CuBiS}_2\text{Cl}_2$ exhibits enhanced stability over LHPs. To verify this, we first carried out thermogravimetric and differential thermal analysis (TGA/DTA). As shown in Figure 4b, weight loss starts at about 300°C ensuring that $\text{CuBiS}_2\text{Cl}_2$ is stable against thermal decomposition for PV applications.

To evaluate the stability against moisture, the $\text{CuBiS}_2\text{Cl}_2$ samples (chunks of about 0.5 mm in size) were stored at room temperature in air with controlled 60% relative humidity. As seen in Figure 4c, the material is reasonably stable by maintaining the XRD pattern after storing for 25 days, which is superior to the LHPs. After 25 days, several peaks in the XRD pattern become more prominent and they are attributed to the formation of BiOCl on the surfaces.^[62] Note that minor BiOCl peaks already exist in the XRD pattern before the aging experiment, i.e., the 0-day sample in Figure 4c, suggesting that surface oxidation may need attention in future studies when making thin-film solar cells.

For a demonstration, we fabricated prototype solar cells based on $\text{CuBiS}_2\text{Cl}_2$ powders. The device structure is shown in the inset of Figure 5 (see the Experimental Section for details of fabrication). Figure 5 shows a typical measured J - V curve, where the short-circuit current density (J_{sc}), open-circuit voltage (V_{oc}) and filling factor (FF) are 1.38 mA cm^{-2} , 1.09 V and 0.66 , respectively, yielding the PCE of 1.00% . We confirmed that the material remains unchanged after the device testing by XRD (see Figure S8, Supporting Information). Without dedicated optimization, the preliminary result, especially the large V_{oc} , which is only 0.35 eV lower than the band gap, is encouraging. The low PCE may be resulted from the low quality of $\text{CuBiS}_2\text{Cl}_2$ film and the contacts. Other important factors to be optimized are the choices of electron and hole transport layers, as well as the interfaces, which are worthy of dedicated studies

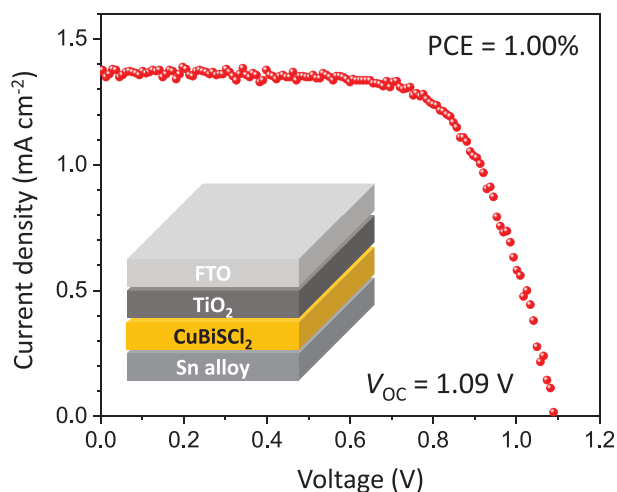


Figure 5. J - V curve measured on a CuBiS_2 based solar cell. The inset shows the schematic structure of the device.

in the future. Overall, the large V_{oc} and reasonable initial efficiency suggest the potential of CuBiS_2 as a promising PV material.

3. Conclusion

In summary, we combined computational screening and experimental synthesis to explore the stable and lead-free PV materials with defect tolerance. Employing three screening criteria of cations with large atomic numbers and lone-pair electrons, mixture of chalcogen and halogen anions and direct band gap with optimal gap value, we screened inorganic materials database and identified CuBiS_2 with a post-perovskite structure for PV applications. Our electronic structure and defect calculations suggest defect tolerance of this material. We synthesized CuBiS_2 and showed that it exhibits strong optical absorption with an onset near 1.44 eV and satisfactory thermal and environmental stability. We also observed a large open circuit voltage of ≈ 1.09 V with a PCE of 1.00% in CuBiS_2 based prototype solar cells. With its optoelectronic properties and stability, CuBiS_2 is expected to be a promising candidate for PV applications. Furthermore, our results suggest that the mixed anion perovskites and related materials could be a direction worth further exploration in the future.

4. Experimental Section

Calculations: The first-principles calculations were based on the density functional theory (DFT) as implemented in the VASP program.^[63] Projector augmented wave (PAW) potentials were used to describe the core-valence interaction.^[64] In the screening calculation, the PBE functional was first employed to calculate the band structure based on the atomic structures from the Materials Project database.^[54] Plane waves with kinetic energy up to 350 eV were used as the basis set. The number of k points was selected as $k_i \times L_i \approx 40$, where k_i and L_i are the number of k points and the length of the basis vector in Å along the i -th direction. The HSE functional^[65] with the inclusion of spin-orbit coupling (SOC) was then used to confirm the band gap for the obtained candidates from the PBE screening.

The atomic structure of CuBiS_2 was relaxed based on the PBE functional with the inclusion of SOC which was relaxed until the residual forces on all atoms were smaller than 0.01 eV \AA^{-1} . The electronic structure was then calculated by the HSE hybrid functional with SOC included.^[65] The COHP calculation^[59] was based on the PBE calculation. Γ -centered $4 \times 4 \times 3$ and $8 \times 8 \times 4$ k -point grids were used for the structural relaxation and electronic structure calculations, respectively.

The defect calculation was based on a $3 \times 1 \times 2$ supercell containing 120 atoms. The defect structures were relaxed with PBE+SOC. Then the single-point calculations were performed with HSE+SOC to obtain the total energy, based on which the transition levels were determined. To calculate the defect formation energy, the stable chemical potential region of CuBiS_2 at the equilibrium growth condition was determined. The formation of CuBiS_2 means that

$$\mu_{\text{Cu}} + \mu_{\text{Bi}} + \mu_{\text{S}} + 2\mu_{\text{Cl}} = \Delta H_f \quad (1)$$

where μ_i is the chemical potential of element i and ΔH_f is the formation energy of CuBiS_2 which was calculated to be -2.81 eV by PBE+SOC. The synthesis of CuBiS_2 from the binary reactants in the experiment means

$$\mu_{\text{Cu}} + \mu_{\text{Cl}} < \Delta H_f(\text{CuCl}) \quad (2)$$

$$2\mu_{\text{Bi}} + 3\mu_{\text{S}} < \Delta H_f(\text{Bi}_2\text{S}_3) \quad (3)$$

$$\mu_{\text{Bi}} + 3\mu_{\text{Cl}} < \Delta H_f(\text{BiCl}_3) \quad (4)$$

The formation energy of CuCl , Bi_2S_3 , and BiCl_3 was calculated to be -0.83 , -1.4 and -3.69 eV, respectively. Eq. (1)–(4) determines the stable chemical potential region of CuBiS_2 , which was plotted in Figure S4 (Supporting Information), where points A and B label the S-rich and S-poor conditions, respectively, used in the defect formation energy calculations.

Synthesis: Polycrystalline samples of CuBiS_2 were prepared by a solid-state reaction. In a glove box under argon atmosphere, the three reactants, CuCl powder (99.999%), BiCl_3 powder (99.99%) and Bi_2S_3 powder (99.9%) were mixed with stoichiometry, ground and pressed into tablets, and sealed in a vacuum quartz tube. The quartz tube was put into a box furnace, which was ramped to 430 °C within 10 h, dwelled for 10 h, cooled down to 200 °C within 60 h, and then turned off to allow the tube to naturally cool down to room temperature.

Characterization: A Bruker D8 Advance X-ray diffractometer with $\text{Cu K}\alpha$ radiation was used to analyze the structure. The microstructures and elemental maps were characterized using a scanning electron microscope (SEM, ZEISS Supra 55) equipped with an energy dispersive spectrometer (EDS). Thermogravimetric and differential thermal analysis (TGA/DTA) on the CuBiS_2 powder sample in nitrogen atmosphere was carried out on a thermal analysis instrument (NETZSCH STA449F3). The sample was heated from 20 to 800 °C with a rate of 10.0 °C min^{-1} . The environmental stability was measured by storing the samples (chunks of ≈ 0.5 mm size) in a temperature and humidity chamber (espec SH-641) with temperature and relative humidity set at 300 K and 60% , respectively, for 25 days.

The optical absorption measurement by transmission was conducted with a Horiba Jobin Yvon confocal Raman microscope with a 600 g mm^{-1} grating. A white lamp was applied as a light source below the sample. Transmitted light was collected using a $100 \times$ ($\text{NA} = 0.9$) microscope lens above the sample. The high NA lens was used to reduce the impact of light scattering. 532 nm long pass filter was inserted to let light below 2.33 eV to pass through. All measurements were performed at ambient condition. A clean glass slide was used as a reference. Measurement was carried out at a $3 \mu\text{m}$ thick sample made by focused ion beam (FEI VERSA3D) etching, which was loaded on the same kind of glass substrate.

Device Fabrication: We dispersed CuBiS_2 powder in the terpene oil solution, scrape-coated the suspension onto the TiO_2/FTO substrate, and dried it at 100 °C for 20 min to remove the solvent, which was

followed by annealing in a tube furnace at 100 °C for 6 h. All the processes were conducted in air. The TiO₂ film is compact with a thickness of ≈30 nm. Then, a Sn-alloy electrode was pressed on the CuBiSCl₂ layer to form a complete solar cell, with an active area of ≈0.5 mm² (estimated by electrode contact area).

Supporting Information

Supporting Information is available from the Wiley Online Library or from the author.

Acknowledgements

C.M., Z.C., F.Z., and S.G. contributed equally to this work. Y.Y.S. acknowledges the support by National Key Research and Development Program of China (2019YFE0103500), National Natural Science Foundation of China (11774365), Shanghai International Cooperation Project (20520760900), and the Major Science and Technology Programs of Yunnan (202002AB080001-1). C.M. acknowledges the support by Natural Science Foundation of Shanghai (19ZR1421800). Z.C., J.J., and J.S. thank the support from US National Science Foundation (NSF) under award No. 1706815. The work at UNCC was supported by ARO/Physical Properties of Materials (Grant No. W911NF-18-1-0079). F.Z. acknowledges the Guangdong Basic and Applied Basic Research Foundation (2021A1515110170). S.Z. acknowledges the support by US NSF EPMD-2042126 and Stampede supercomputer resources at TACC made available by XSEDE through allocation TG-DMR180114, which was supported by NSF Grant Number ACI-1548562.

Conflict of Interest

The authors declare no conflict of interest.

Data Availability Statement

The data that support the findings of this study are available from the corresponding author upon reasonable request.

Keywords

computational screening, defect tolerance, lead-free perovskites, optical absorption, photovoltaics

Received: December 10, 2021

Revised: January 26, 2022

Published online:

- [1] M. A. Green, A. Ho-Baillie, H. J. Snaith, *Nat. Photonics* **2014**, *8*, 506.
- [2] A. Kojima, K. Teshima, Y. Shirai, T. Miyasaka, *J. Am. Chem. Soc.* **2009**, *131*, 6050.
- [3] H. Min, D. Y. Lee, J. Kim, G. Kim, K. S. Lee, J. Kim, M. J. Paik, Y. K. Kim, K. S. Kim, M. G. Kim, T. J. Shin, S. Il Seok, *Nature* **2021**, *598*, 444.
- [4] N. J. Jeon, J. H. Noh, Y. C. Kim, W. S. Yang, S. Ryu, S. I. Seok, *Nat. Mater.* **2014**, *13*, 897.
- [5] Z. Li, T. R. Klein, D. H. Kim, M. Yang, J. J. Berry, M. F. A. M. van Hest, K. Zhu, *Nat. Rev. Mater.* **2018**, *3*, 18017.
- [6] Z.-K. Tan, R. S. Moghaddam, M. L. Lai, P. Docampo, R. Higler, F. Deschler, M. Price, A. Sadhanala, L. M. Pazos, D. Credgington, F. Hanusch, T. Bein, H. J. Snaith, R. H. Friend, *Nat. Nanotechnol.* **2014**, *9*, 687.
- [7] S. D. Stranks, H. J. Snaith, *Nat. Nanotechnol.* **2015**, *10*, 391.
- [8] Q. Chen, J. Wu, X. Ou, B. Huang, J. Almutlaq, A. A. Zhumeckenov, X. Guan, S. Han, L. Liang, Z. Yi, J. Li, X. Xie, Y. Wang, Y. Li, D. Fan, D. B. L. Teh, A. H. All, O. F. Mohammed, O. M. Bakr, T. Wu, M. Bettinelli, H. Yang, W. Huang, X. Liu, *Nature* **2018**, *561*, 88.
- [9] J. Zhao, L. Zhao, Y. Deng, X. Xiao, Z. Ni, S. Xu, J. Huang, *Nat. Photonics* **2020**, *14*, 612.
- [10] N. Glück, T. Bein, *Energy Environ. Sci.* **2020**, *13*, 4691.
- [11] F. De Angelis, *ACS Energy Lett.* **2021**, *6*, 1586.
- [12] R. Nie, R. R. Sumukam, S. H. Reddy, M. Banavoth, S. I. Seok, *Energy Environ. Sci.* **2020**, *13*, 2363.
- [13] Z. Xiao, Z. Song, Y. Yan, *Adv. Mater.* **2019**, *31*, 1803792.
- [14] I. Chung, J.-H. Song, J. Im, J. Androulakis, C. D. Malliakas, H. Li, A. J. Freeman, J. T. Kenney, M. G. Kanatzidis, *J. Am. Chem. Soc.* **2012**, *134*, 8579.
- [15] X.-G. Zhao, J.-H. Yang, Y. Fu, D. Yang, Q. Xu, L. Yu, S.-H. Wei, L. Zhang, *J. Am. Chem. Soc.* **2017**, *139*, 2630.
- [16] Z. Xiao, K.-Z. Du, W. Meng, J. Wang, D. B. Mitzi, Y. Yan, *J. Am. Chem. Soc.* **2017**, *139*, 6054.
- [17] A. H. Slavney, T. Hu, A. M. Lindenberg, H. I. Karunadasa, *J. Am. Chem. Soc.* **2016**, *138*, 2138.
- [18] C. N. Savory, A. Walsh, D. O. Scanlon, *ACS Energy Lett.* **2016**, *1*, 949.
- [19] P. Cheng, T. Wu, J. Liu, W.-Q. Deng, K. Han, *J. Phys. Chem. Lett.* **2018**, *9*, 2518.
- [20] P. Cheng, T. Wu, J. Zhang, Y. Li, J. Liu, L. Jiang, X. Mao, R.-F. Lu, W.-Q. Deng, K. Han, *J. Phys. Chem. Lett.* **2017**, *8*, 4402.
- [21] M. B. Johansson, H. Zhu, E. M. J. Johansson, *J. Phys. Chem. Lett.* **2016**, *7*, 3467.
- [22] B. Saparov, F. Hong, J. P. Sun, H. S. Duan, D. B. Mitzi, *Chem. Mater.* **2015**, *27*, 5622.
- [23] Y. Y. Sun, M. L. Agiorgousis, P. Zhang, S. Zhang, *Nano Lett.* **2015**, *15*, 581.
- [24] S. Perera, H. Hui, C. Zhao, H. Xue, F. Sun, C. Deng, N. Gross, C. Milleville, X. Xu, D. F. Watson, B. Weinstein, Y.-Y. Sun, S. Zhang, H. Zeng, *Nano Energy* **2016**, *22*, 129.
- [25] X. Wei, H. Hui, C. Zhao, C. Deng, M. Han, Z. Yu, A. Sheng, P. Roy, A. Chen, J. Lin, D. F. Watson, Y.-Y. Sun, T. Thomay, S. Yang, Q. Jia, S. Zhang, H. Zeng, *Nano Energy* **2020**, *68*, 104317.
- [26] Z. Yu, X. Wei, Y. Zheng, H. Hui, M. Bian, S. Dhole, J.-H. Seo, Y.-Y. Sun, Q. Jia, S. Zhang, S. Yang, H. Zeng, *Nano Energy* **2021**, *85*, 105959.
- [27] S. Niu, H. Hui, Y. Liu, M. Yeung, K. Ye, L. Blankemeier, T. Orvis, D. Sarkar, D. J. Singh, R. Kapadia, J. Ravichandran, *Adv. Mater.* **2017**, *29*, 1604733.
- [28] S. Niu, D. Sarkar, K. Williams, Y. Zhou, Y. Li, E. Bianco, H. Hui, S. B. Cronin, M. E. McConney, R. Haiges, R. Jaramillo, D. J. Singh, W. A. Tisdale, R. Kapadia, J. Ravichandran, *Chem. Mater.* **2018**, *30*, 4882.
- [29] W. Meng, B. Saparov, F. Hong, J. Wang, D. B. Mitzi, Y. Yan, *Chem. Mater.* **2016**, *28*, 821.
- [30] C. Ming, K. Yang, H. Zeng, S. Zhang, Y.-Y. Sun, *Mater. Horiz.* **2020**, *7*, 2985.
- [31] D. Meggiolaro, F. De Angelis, *ACS Energy Lett.* **2018**, *3*, 2206.
- [32] R. E. Brandt, V. Stevanović, D. S. Ginley, T. Buonassisi, *MRS Commun.* **2015**, *5*, 265.
- [33] J. Kang, L.-W. Wang, *J. Phys. Chem. Lett.* **2017**, *8*, 489.
- [34] F. Brivio, K. T. Butler, A. Walsh, M. van Schilfegaarde, *Phys. Rev. B* **2014**, *89*, 155204.
- [35] P. Umari, E. Mosconi, F. De Angelis, *Sci. Rep.* **2014**, *4*, 4467.
- [36] W.-J. Yin, T. Shi, Y. Yan, *Appl. Phys. Lett.* **2014**, *104*, 063903.

- [37] M. L. Agiorgousis, Y.-Y. Sun, H. Zeng, S. Zhang, *J. Am. Chem. Soc.* **2014**, *136*, 14570.
- [38] M. H. Du, *J. Phys. Chem. Lett.* **2015**, *6*, 1461.
- [39] J. Kang, J. Li, S.-H. Wei, *Appl. Phys. Rev.* **2021**, *8*, 031302.
- [40] C. Ming, H. Wang, D. West, S. Zhang, Y.-Y. Sun, *J. Mater. Chem. A* **2022**, *10*, 3018.
- [41] N. Onoda-Yamamuro, T. Matsuo, H. Suga, *J. Phys. Chem. Solids* **1992**, *53*, 935.
- [42] Q. Lin, A. Armin, R. C. R. Nagiri, P. L. Burn, P. Meredith, *Nat. Photonics* **2015**, *9*, 106.
- [43] X. He, D. J. Singh, P. Boon-on, M.-W. Lee, L. Zhang, *J. Am. Chem. Soc.* **2018**, *140*, 18058.
- [44] N. Gross, Y.-Y. Sun, S. Perera, H. Hui, X. Wei, S. Zhang, H. Zeng, B. A. Weinstein, *Phys. Rev. Appl.* **2017**, *8*, 044014.
- [45] T. Gupta, D. Ghoshal, A. Yoshimura, S. Basu, P. K. Chow, A. S. Lakhnot, J. Pandey, J. M. Warrender, H. Efstathiadis, A. Soni, E. Osei-Agyemang, G. Balasubramanian, S. Zhang, S. F. Shi, T. M. Lu, V. Meunier, N. Koratkar, *Adv. Funct. Mater.* **2020**, *30*, 2001387.
- [46] S. Niu, J. Milam-Guerrero, Y. Zhou, K. Ye, B. Zhao, B. C. Melot, J. Ravichandran, *J. Mater. Res.* **2018**, *33*, 4135.
- [47] Y.-Y. Sun, J. Shi, J. Lian, W. Gao, M. L. Agiorgousis, P. Zhang, S. Zhang, *Nanoscale* **2016**, *8*, 6284.
- [48] A. M. Ganose, K. T. Butler, A. Walsh, D. O. Scanlon, *J. Mater. Chem. A* **2016**, *4*, 2060.
- [49] R. Nie, A. Mehta, B.-w. Park, H.-W. Kwon, J. Im, S. I. Seok, *J. Am. Chem. Soc.* **2018**, *140*, 872.
- [50] T. Li, X. Wang, Y. Yan, D. B. Mitzi, *J. Phys. Chem. Lett.* **2018**, *9*, 3829.
- [51] R. Nie, J. Im, S. I. Seok, *Adv. Mater.* **2019**, *31*, 1808344.
- [52] R. Nie, H.-S. Yun, M.-J. Paik, A. Mehta, B.-W. Park, Y. C. Choi, S. I. Seok, *Adv. Energy Mater.* **2018**, *8*, 1701901.
- [53] H. Kageyama, K. Hayashi, K. Maeda, J. P. Attfield, Z. Hiroi, J. M. Rondinelli, K. R. Poeppelmeier, *Nat. Commun.* **2018**, *9*, 772.
- [54] A. Jain, S. P. Ong, G. Hautier, W. Chen, W. D. Richards, S. Dacek, S. Cholia, D. Gunter, D. Skinner, G. Ceder, K. A. Persson, *APL Mater.* **2013**, *1*, 011002.
- [55] W. Shockley, H. J. Queisser, *J. Appl. Phys.* **1961**, *32*, 510.
- [56] M. Murakami, K. Hirose, K. Kawamura, N. Sata, Y. Ohishi, *Science* **2004**, *304*, 855.
- [57] A. R. Oganov, S. Ono, *Nature* **2004**, *430*, 445.
- [58] M. Ruck, P. Poudeu, T. SöHnel, *Z. Anorg. Allg. Chem.* **2004**, *630*, 63.
- [59] S. Steinberg, R. Dronskowski, *Crystals* **2018**, *8*, 225.
- [60] P. A. Fernandes, P. M. P. Salomé, A. F. da Cunha, *Semicond. Sci. Technol.* **2009**, *24*, 105013.
- [61] X. Wu, W. Gao, J. Chai, C. Ming, M. Chen, H. Zeng, P. Zhang, S. Zhang, Y.-Y. Sun, *Sci. China Mater.* **2021**, *64*, 2976.
- [62] L. Kan, Y. Tang, Y. Xu, Y. Wang, J. Jia, *Appl. Catal., B* **2013**, *140–141*, 179.
- [63] G. Kresse, J. Furthmüller, *Comput. Mater. Sci.* **1996**, *6*, 15.
- [64] G. Kresse, D. Joubert, *Phys. Rev. B* **1999**, *59*, 1758.
- [65] J. Heyd, G. E. Scuseria, M. Ernzerhof, *J. Chem. Phys.* **2003**, *118*, 8207.